



VLASS Project Memo #13:

Pilot and Quick Look Data Release (v2)

M. Lacy, S. T. Myers, C. Chandler, A. D. Kapinska, B. Kent, A. Kimball, J. Marvil, J. Masters, D. Medlin, K. Radford, F. Schinzel, L. Sjouwerman, A. Sobotka, A. Vargas (NRAO)

June 16, 2022

The Very Large Array Sky Survey (VLASS) produces “Quick Look” image products using a simple imaging algorithm as rapidly as possible after the data are taken, in order to enable searches for transient objects. In this Memo we describe and characterize the Quick Look image products from the VLASS Pilot survey observed in 2016, and the first two epochs of VLASS (campaigns VLASS1.1, VLASS1.2, VLASS2.1, VLASS2.2). Apart from VLASS1.1, which suffered from an antenna pointing error that affected 2/3 of the antennas, the integrated flux densities are within 3% of the Perley-Butler scale. Peak flux density measurements are low by $\approx 8\%$ due to residual phase errors. For VLASS1.1, the corresponding flux densities are low by $\approx 10\%$ for integrated flux densities and $\approx 15\%$ for peak flux densities. Above 1 Jy the flux densities in VLASS 1.1 can be very unreliable and should not be used. In addition, in a small number of cases throughout the Epoch 1 images, we discovered artifacts (“ghost sources”) introduced by various online system errors during observing. These have been excised from the QL data and images to some extent, but some undiscovered ghosts issues may remain, especially for faint sources. Epoch 2 is unaffected by these ghosts. Position errors, present in the first release of Epoch 1, have now been fixed and corrected Epoch 1 images are available. *This Memo has been updated since its original publication in 2019 to reflect improved understanding of the position and calibration issues with QL imaging and to include Epoch 2.*

Contents

1	Introduction	2
2	Quicklook Calibration — Quality Assurance and Issues	3
2.1	Quicklook Calibration and Quality Assurance	3
2.2	Issue: Antenna pointing corrections	4
2.3	Issue: Delay center errors	5
2.3.1	Flagging data for delay-center errors	6
2.4	Issue: Polarization calibration in the Pilot	8
3	Quick-Look Imaging	9
3.1	Quick-Look Image Pipeline and Quality Assurance	9
3.1.1	Quick-Look Imaging Creation & Parameters	10
3.1.2	Creation of Noise Images	11
3.2	Issues found in QL imaging	11
3.2.1	Issue: Imaging Divergence	11
3.2.2	Issues: Ghost sources	12
3.2.3	Issue: Pointing Offsets	16
3.2.4	Issue: W-Term	16
3.3	Quick Look image quality	16
3.3.1	Quick Look positional accuracy	17
3.3.2	Quick Look flux density accuracy	17
3.3.3	Sensitivity	20
3.3.4	Quick Look image artifacts	21
4	Summary	21
A	Case Studies for Out-of-Order (OOO) Events	24
A.1	Case IIIb	24
A.2	Case IIb	26

1. Introduction

The data release plan for VLASS calls for “Quick Look” (QL) images to be made available within a short timescale of observation (goal of one week, requirement of two weeks) to aid with searches for transients. This memo characterizes the calibration and QL imaging products for the VLASS pilot observations and the first two epochs of VLASS (the VLASS1.1 VLASS1.2, VLASS2.1 and VLASS2.2 observing campaigns). Future memos will describe the set of higher quality products resulting from Single Epoch and Cumulative Epoch processings, which will use more accurate imaging techniques.

The VLASS Pilot survey¹ was observed from June to September 2016. The observations were designed to map key areas needed to inform the final survey design and provide observations of well-studied fields that enable comparison with prior data, both at radio and other wavelengths. The Pilot was also used to test the observing strategy and setup. It used 196 hr of VLA time and covered 2480 deg² of sky. The Pilot survey includes both single scans and full depth (three repeats within the 4-month duration of the B-configuration in which the pilot was observed) on a set of well-studied fields, selected to contain complementary data at radio and/or other wavelengths. Raw visibility data and calibration products for data taken during the Pilot are available for download in the NRAO archive under project code TSKY0001 (see <https://science.nrao.edu/science/surveys/vlass/> for information on how to identify the pilot scheduling blocks in the archive). Quick Look images from the Pilot are available through the same web interface as the VLASS Epoch 1 and 2 Quick Look images.

The first half of the first epoch of VLASS was observed from September 2017 to February 2018, and is stored under project VLASS1.1 in the NRAO archive. The second half of the first epoch was observed from March 2019 to July 2019, and is stored under project code VLASS1.2. The second epoch was observed in VLASS2.1 (June 2020 – November 2020) and VLASS2.2 (September 2021 – February 2022). VLASS2.1 overlapped with VLASS1.1 and VLASS2.2 with VLASS1.2.

The overall VLASS calibration strategy is described in [2]. In this memo we first describe specific calibration issues that affected only the pilot and the first epoch of VLASS, then characterize the Stokes I continuum products produced by the QL imaging pipeline.

2. Quicklook Calibration — Quality Assurance and Issues

2.1. Quicklook Calibration and Quality Assurance

The VLASS data were calibrated using an automated pipeline. The processing of the data is controlled through a Survey Manager interface, that combines the database and workflow used to run the CASA pipeline and to track the status of jobs. The calibration pipeline uses measurements on known intensity and polarization calibration sources, as well as measurements of system responses (e.g. the switched and total power of antennas) and transfers these to the OTF mosaic data. RFI flagging, flagging for data without calibration solutions, and any flagging set up-front for known issues, are also determined and applied. Paper 1 contains a description of the calibration process and limitations.

After calibration pipeline completion, the pipeline “weblogs” were examined as part of the Quality Assurance (QA) process by the VLASS Data Analyst (DA) team. Recommendations based on this examination were made to “Accept & Archive” (and continue to imaging), to rerun (e.g. with additional flagging or other changes), or to “Reject” and re-observe if irrecoverable errors were found (usually due to inclement weather or missing

¹<https://go.nrao.edu/vlass-memo002>

calibration scans). After the DA carried out any pipeline re-runs, the calibrations were usually Accepted. If problems or concerns remained, information about the calibration was forwarded to the staff "Astronomer on Duty" (AoD) for Calibration, who made the final decision on whether to Accept, carry out further re-executions, or Reject and re-observe all or part of the block. (During VLASS1.1, all calibrations were examined by the AOD, however, by the later campaigns training of the DAs had improved so as to render this unnecessary.)

Typical issues that required re-execution of the pipeline include problems with the reference antenna used in the calibration, radio frequency interference (RFI) on the calibrator scans compromising the calibration solutions, delay center errors on calibrations scans, and similar issues. In addition, as described in Paper 1, RFI for observations taken near the geostationary satellite belt often exhibit gain compression, which necessitates re-running the pipeline with compression calibration turned on. Other issues, such as the ghost-producing errors in OTF scans described below, require additional flags to be applied to the data (these flags are also re-ingested into the archive), but do not require the calibration pipeline to be re-run.

The target flagging heuristics for Quick Look varied slightly between observing campaigns. In particular, in VLASS2.1, the RFI flagging was increased and flags "grown" around flagged data points. This was found to have a detrimental effect on the noise (at the $\approx 10 - 20\%$ level) without helping noticeably with artifact suppression, so the flag growth was removed for Single Epoch imaging for all epochs, and Quick Look imaging from VLASS2.2 onwards.

2.2. Issue: Antenna pointing corrections

The antenna pointing data recorded in the pointing tables of the raw Science Data Model (SDM) files were incorrect for the pilot survey and for the first half of the first epoch (VLASS1.1). For the pilot processing, the pointing table had erroneous entries and had to be removed completely prior to processing. We expect this to have little impact on QL images as the pointing uncertainty is less than ≈ 0.1 of the primary beam FWHM, and, indeed, in VLASS Memo 17 we confirm that the use of the pointing tables results in only a small improvement in dynamic range. However, during VLASS1.1 (only) all antennas with old-style Antenna Control Units (ACUs, comprising around 2/3 of the antennas during VLASS1.1) were mis-pointed due to an error in the timing for commands sent to those ACUs, and had a pointing table that did not reflect the true pointing direction but only the direction that the executor was using (see VLASS Memo #12² for a more detailed description of the problem). This pointing offset affected both derived flux densities and in-band spectral indices. The pointing tables will be corrected before the Single Epoch imaging is undertaken for VLASS1.1.

²<http://go.nrao.edu/vlass-memo012>

2.3. *Issue: Delay center errors*

Table 1 summarizes the dates for which various problems relating to delay models were experienced for the pilot, VLASS1.1, and VLASS1.2. The following paragraphs provide more detail on these issues.

Throughout the Pilot, VLASS1.1, and VLASS1.2, various online system problems resulted in occasional incorrect delay centers being used by the correlator during parts of an On-The-Fly (OTF) mosaic scan, resulting in the position used by the correlator being different from that recorded in the SDM metadata. These data, when imaged, cause copies (or “ghosts”) of any sources in that field to appear, offset from their true positions; see Section 3.2.2 below for further details of how ghosts are diagnosed and corrected. This problem was first identified early during VLASS1.1 observing by colleagues from Caltech (D. Dong and G. Hallinan), when searching the Pilot and VLASS1.1 for transients compared to the FIRST survey catalog. In some cases, the problem resulted in a characteristic signature in the visibility data, whereby an incorrect number of integrations had been assigned to each phase center (i.e., each Field in the MeasurementSet, or MS). These could be identified and flagged before imaging. However, the majority of cases could only be identified during imaging, with no other signatures seen in the SDM or MS metadata. These events could (and did) occur at any point in an OTF scan.

The origin of the problem described above was identified and a bug fix deployed in the online system on November 15, 2017. No ghosts of the kind described above were seen for the rest of VLASS1.1. However, the solution introduced a potential race condition where occasionally an “Out-Of-Order” (OOO) delay model was queued for use in the correlator within the first 10 seconds of the start of an OTF row. This issue was only discovered during VLASS1.2 observing and corrected in the online system on June 13, 2019. This problem has likely existed since November 15, 2017, and can affect the first 11 phase-centers in an OTF scan in two different ways (see below).

When the race condition is present with the version of the correlator monitor/control interface board (CMIB) software deployed from November 15, 2017 until March 14, 2019, and re-deployed on May 13, 2019, the 11th phase center (9.9sec into the OTF scan) would receive an OOO command and be correlated with the position of the scan from 10 seconds earlier (the backup scan just before the OTF row, around 30 arc-minutes away). Because of this large offset, the ghosts were attenuated by the mosaic imaging software and not visible in the quick-look images.

However, an update to the CMIB software was deployed on March 14, 2019, to try to fix issues experienced by other (non-VLASS) observers due to the delay-model “look-ahead” introduced in November 2017 to fix the VLASS ghosting issue. This CMIB software, when combined with the executor race condition described above, caused ghosts to possibly appear within the first 10 seconds of OTF rows for observations made from March 15, 2019 until May 13, 2019 at which point the CMIB software was rolled back to the pre-March version (with the behavior reverting to that during the previous period). In a very small number of instances in this same time range, a similar effect was seen in calibrator

scans with phase jumps usually lasting 10s before returning to nominal phase. These were identified and flagged (and the data re-calibrated, if deemed serious enough to impact QL imaging). From April 12 onward, Out-of-Order events were logged in the system, and we were provided an number of instances to check for issues (see below).

From May 14, 2019, until June 13, 2019, the system behavior was the same as during the period from November 15, 2017, until March 14, 2019. On June 14, 2019, the executor software was fixed to remove the race condition issue. Subsequent to this, no ghosts nor reports of the race condition were logged (the last OOO command was logged on 2019-06-13 at 14:58:13.9 UT). No similar issues were seen in VLASS2.1 and VLASS2.2 observations.

Table 1: Summary of symptoms and dates affected by delay problems in the VLASS pilot, VLASS1.1, and VLASS1.2

Date range	Case & Symptom
2016-Jun-10 through 2017-Nov-14	I. Ghost sources caused by Executor intermittently falling behind sending delay models to correlator (Pilot, VLASS1.1)
2017-Nov-15 through 2019-Mar-14	IIa. Occasional executor race condition in command queuing causing 11th OTF phase-center to be correlated at position 10s earlier; no ghosts visible in mosaics (VLASS1.1, VLASS1.2)
2019-Mar-15 through 2019-Apr-11	IIIa. CMIB software update combined with race condition causing occasional phase jump lasting 10s on calibrator scans, and ghosts during first 11 OTF phase-centers (VLASS1.2)
2019-Apr-12 through 2019-May-13	IIIb. CMIB issue combined with race condition as in IIIa but with race condition occurrences logged (VLASS1.2)
2019-May-14 through 2019-Jun-13	IIb. CMIB software reverted to pre-14-Mar version, symptom as in case IIa above (VLASS1.2)
2019-Jun-14 onward	IV. executor race condition fixed; no known issues (VLASS1.2)

2.3.1. Flagging data for delay-center errors

The impact of undetected ghosts on the mosaic images is primarily that these fields (even if they do not produce visible ghost sources) will not contribute coherently to the image, and thus any sources in these regions will be depressed in flux density by a significant factor. Tests based on a few VLASS1.2 datasets show this effect to be as high as 25% in flux density where the source lies in the center of the fields affected. Therefore, it is important to remove data that is known to — or due to the limitations of logging information, could possibly be — affected by the issues listed above.

The first release of QL images for the VLASS1.1 and VLASS1.2 data were produced as quickly as possible before full knowledge of the extent of the ghosting and race condition

issues were understood. We have since gone back and flagged and reimaged the data known to be affected by these problems, and they have been ingested into the NRAO archive and placed in the cache area for online access. The QL images were produced from data that has been flagged for issues found during QA inspection, and in a few cases in VLASS1.2 examples of the above that were found during testing were flagged also.

For data taken before November 15, 2017, which includes the Pilot and a portion of VLASS1.1 (case I symptoms in Table 1), delay center errors were sporadic and random in occurrence, and we rely upon identification of ghosts in the mosaic images during imaging QA to identify cases to flag. In addition, during this period, examination of the *listobs* output with a script (`checkscans.py`) by the DAs was able to find cases where an incorrect number of visibilities (INoV) were assigned to some phase centers, which in some cases is an indication of possible ghost events. For example, while it is common to have 3 integrations in the last field of an OTF scan due to timing considerations, and it is also fairly common to have a single field with a single integration in the middle of a scan without ghost issues, all other instances were deemed to be ghosts and flagged. Note that not all visible ghosts are associated with INoV events.

For observations taken from April 12, 2019, onward until the end of VLASS1.2 in July 2019, a period that covers part of the time when the errant CMIB software was deployed, the issuance of delay models by the system to a single antenna were monitored and recorded. Logging was started on 2019-Apr-11 at 21:46:53UT, and from this time onward, instances of OOO events from the race condition were identified. This feature allowed us to diagnose the problem. However, statistics (see § 3.2.2) revealed that for Case IIIb only about half of the reported OOO events showed ghosting behavior. In addition, 64% of the identified ghosts corresponded to OOO events, although all observed ghosts fell within the first 11 fields of an OTF row.

This behavior was also borne out in detailed testing of a small number of events (see Appendix A). Therefore, to be conservative, we plan to flag for all of Case III the first 11 fields of each OTF row. This will cause sensitivity loss for images at the East and West edges of tiles, but avoids possible ghost effects. Although our tests for Case IIb OOO events indicated that every one examined showed ghosting behavior (if sources could be seen), we cannot at this time preclude the possibility that there are ghosting events in the 11th field that do not correspond to OOO events. Thus, for both Case IIa (without logging) and Case IIb, we will flag the 11th field of each OTF row.

For the Case II and III images made promptly as part of QL Release 0, as for the Case I described above, the visible ghosts found by imaging QA and events with INoV (only 4 were seen in Case IIIa) were flagged. For a few cases where the QL data was on-disk when OOO logging was present, these events were also flagged, as well as extra ghosts identified during the testing.

Our actions for flagging before Single-Epoch imaging and for re-imaging for any future QL release are informed by the above considerations, and the analysis of images described below in § 3.2.2. Based on this:

- For Case I taken before November 15, 2017, identified cases of ghosts and INoV are flagged. There is no additional flagging to be done, unless we develop better ghost recognition algorithms.
- For Case II for the period from November 15, 2017, until March 13, 2019 (Case IIa) and May 14 to June 13, 2019, we will flag the 11th phase-center of each OTF scan in the data.
- For Case III for March 15 through May 13, 2019 (Case IIIa and Case IIIb) the first 11 phase-centers of each OTF could potentially be ghosted, and we will flag the first 11 fields of every OTF row during this time.
- For Case IV observations taken from June 14 onward, no race conditions were logged, nor ghosts seen in the images, and no extra flagging is deemed warranted.

Table 2 contains a summary of the flags to be applied to the data before final SE imaging or a QL Release 1, as well as the status of flagging for QL Release 0.

Table 2: Summary of flagging to be applied for Single-Epoch imaging based on the delay center errors (ghosts and logged Out-Of-Order events) for Pilot, VLASS1.1, and VLASS1.2. Final column is whether QL “Release 0” images have been flagged for issues as of this memo date (INoV refers to “incorrect number of visibilities”, G means visible ghosts only, G/P means visible ghosts and partially flagged for logged OOO events). Cases are as in Table 1.

Epoch	Date range	Case	SE Flagging	QLR0
Pilot	2016-Jun-10 – Sep-01	I	Ghosts & INoV	yes
1.1	2017-Sep-08 – Nov-14	I	Ghosts & INoV	yes
1.1	2017-Nov-15 – 2018-Feb-20	IIa	OTF Field 11	yes
1.2	2019-Mar-05 – Mar-14	IIa	OTF Field 11	yes
1.2	2019-Mar-15 – Apr-11	IIIa	Ghosts & OTF Fields 1-11	G
1.2	2019-Apr-12 – May-13	IIIb	Ghosts & OTF Fields 1-11	G/P
1.2	2019-May-14 – Jun-13	IIb	OTF Field 11	yes
1.2	2019-Jun-14 – Jul-16	IV	No problems	n/a

2.4. Issue: Polarization calibration in the Pilot

Although the QL data products do not include polarization images (e.g. cubes in Stokes Q and U), the QL calibrations available from the archive do include full polarization

calibration. For VLASS, the primary position angle calibrator is 3C286. However, in the Pilot survey for parts of the sky where 3C286 was not observable, 3C48 was used as polarization position angle calibrator. Because 3C48 is only weakly polarized at the low end of the VLASS observing frequency range, calibration with 3C48 led to higher uncertainties in polarization angle calibration at 2.0–2.5 GHz with uncertainties of up to $\sim 4^\circ$ in absolute position angle. Furthermore, several tiles did not observe the leakage calibrator over a large enough range in parallactic angle to obtain a correct calibration. We therefore do not intend to produce polarization products for the Pilot, and in other cases there was not enough time on source to obtain viable leakage solutions for 2 MHz channels. In VLASS1.1 and VLASS1.2, these problems were rectified, and if 3C286 was not available, one of two secondary polarization calibrators, 3C138 or J1800+7828, were used. The secondary calibrators are variable, and a time-dependent model may be needed in the Single Epoch calibration pipeline to deal with this variability (though this has not been required for epochs 1 or 2). We strongly caution users against using QL calibration products from the Pilot for polarization studies.

3. Quick-Look Imaging

3.1. Quick-Look Image Pipeline and Quality Assurance

VLASS Quick Look Images are produced in the Quick-Look Imaging Pipeline (QLIP), under a workflow controlled by the Survey Manager. The QLIP uses the CASA task *tclean* with *gridder='mosaic'* using 1-arcsecond pixels (i.e., the Point Spread Function is under-sampled, and there are no corrections for w-terms). These approximations make the imaging fast, but combined with the non-optimal primary beam models used by this gridder, lead to reduced fidelity for these image products as described in Section 3.3. The images are made as 2×2 deg² mosaics, and are subsequently trimmed down to 1×1 deg² to ensure that sources on the edges of the final image products are correctly deconvolved. More accurate Single Epoch images are now being produced, which use self-calibration and provide spectral index information and coarse cubes in Stokes I, Q and U.

The QA process for quick-look imaging involves evaluation of the automatically generated image statistics generated by the QLIP to pre-populate the “QA Notes box” in the Survey Manager, followed by examination of the QLIP weblog. More detailed data sleuthing may be needed for problematic cases, in most cases these are referred by the Data Analysts to an AoD who is on-call to consult on problems as they arise. Possible actions for QL Imaging include “Accept & Archive”, to rerun (e.g. with additional flagging, modified image size, or other changes to imaging parameters), or to “Reject & Archive” if deemed that no further improvements can be made to bring the image above the threshold for acceptance. In general, an image is accepted by QA if the peak residual in the initial mosaic image (in the “flat noise” image before PB correction and the $62' \times 62'$ cutout is made) is less than six times the RMS noise, and is otherwise free from obvious artifacts. Images with peak to RMS ratios higher than this are treated on a case-by-case basis, with

those having peak to RMS ratios >10 very rarely being accepted. Around very bright sources, the visibility weights can be skewed very low by the CASA *statwt* task, creating missing (masked) regions in the images. These images are typically reprocessed with different weighting to correctly image the bright source, but remain rejected by QA as they do not follow the standard processing path (and can be found in the archives under “QA_REJECTED” images for each epoch).

3.1.1. Quick-Look Imaging Creation & Parameters

Quick Look images are created using the CASA task *tclean* with the mosaic gridded. This combines the visibilities taken in the different OTF pointings by gridding into the uv-plane to transform into a single image, which is then deconvolved in the Cotton-Schwab minor cycles before transforming the model back to compute residual images in the next major cycle.

Each tile (usually 4° tall in declination by approximately 10° wide in RA) is broken into $1^\circ \times 1^\circ$ regions for imaging, spaced by 1° in RA on rows of constant Dec. The image centers are placed starting from one edge of the tile, there are typically either ten or eleven centers in RA depending on where the other edge lies. The rows are spaced by 1° in Dec with centers at each :30 in Declination. See VLASS Memo 7 for tile definitions.

Images are made in the QLIP with the following default parameters:

- *gridded* = ‘mosaic’
- *imsize* = 7290
- *cellsize* = ‘1.0arcsec’
- *cycleniter* = 500

In order to have full sensitivity for the central square degree of the mosaic, we select OTF fields with centers that lie within $2800''$ in RA and Dec of the image center, within a search radius controlled by the pipeline parameter

- *search_radius_arcsec* = 1000.0

of the edge of the inner degree. A full image of linear dimension $7290''$ containing the mosaic pointings is processed. After deconvolution, a cutout “subimage” is created with linear dimension of $62'$, providing an overlap of approximately $1'$ between adjacent images.

The purpose of using the mosaic gridded is to be able to create these images quickly. However, there are some shortcomings of this approach that manifest in imaging issues described below. The primary one is that there is no correction for the w-term (see § 3.2.4) using either faceting or w-projection. Another is that, by default, deconvolution is carried out using the Point-Spread Function (PSF) calculated at the image center, and thus PSF variations across the mosaic image will not be accounted for.

3.1.2. Creation of Noise Images

Root mean square deviation (RMSD) images for estimating the noise as a function of position in the VLASS images are supplied as part of the QL data products. These are generated using the CASA task *imdev*, available in CASA version 5.0.0 and following. This task has a variety of algorithms available for estimating the RMSD from a set of pixel values. The one selected for VLASS was the Chauvenet criterion, which eliminates data points that lie outside the expected range for members of a normal distribution of data points.³ The RMSD image is evaluated on a rectangular grid with 20 pixel spacing, using a 60×60 pixel box (both the grid spacing and box size are configurable in the CASA task, and a circle can be used instead of a box). A cubic interpolation is used between grid points, and for extrapolation beyond the edge of the grid.

For VLASS, the full restored clean image (before subimaging to the final $62' \times 62'$ image size) is used as the input to *imdev*, and the output image is also subimaged to $62' \times 62'$. This is so that sources could be more clearly found, excluded, and interpolated over by the algorithm. Tests using the final residual image indicated that the RMSD estimates in pixels occupied by source emission could be biased high or low compared to the surrounding pixels. This also means that except near the image edges, the RMSD image could be recreated from the archived QL restored images. For QL, the RMSD image as described above is stored in the archive, with an image suffix of “.rms.subim.fits”.

3.2. Issues found in QL imaging

3.2.1. Issue: Imaging Divergence

For QL imaging in the Pilot and VLASS1, we use the *tclean* with *gridded*='mosaic' as described in § 3.1.1 above. For images containing sources brighter than around 60 mJy/beam, the deconvolution process can diverge, causing artifacts in the final image, and/or significant uncleaned emission remaining in the residual. We describe some imaging options used to reduce these divergences, but some cases remain.

Divergences are the most frequent failure mode affecting the visual quality for imaging, and occur when errors in the image-plane deconvolution stage (in the minor cycles of imaging using the Cotton-Schwab algorithm) on bright sources causes ever increasing errors not correctable in major cycles. This appears to be primarily due to variations in the PSF over the mosaic causing subtraction of the PSF in the minor cycle to dig negative holes or linear trenches before being caught and aborting the clean process. The main effect of divergences in the QL images is the presence of “sidelobe” artifacts, both residual PSF sidelobes from undeconvolved emission, and anomalous sidelobes from the incorrect PSF being used in the minor cycles of deconvolution). These will also increase the noise level in the image as they spread flux density away from the sources. There may also be a contribution to inaccuracy of the flux densities of sources, especially for extended

³https://en.wikipedia.org/wiki/Chauvenet's_criterion

components.

In this case, reducing the number of minor cycles allowed in each major cycle (*cycleniter*) can help mitigate the divergence, allowing deconvolution to go deeper without aborting, at the cost of performing more major cycles and thus taking a lot longer to complete. Smaller images can be made to help offset this increased time, or to exclude bright sources that diverge at the edges of the full images. Example modified parameters for those described in § 3.1.1 include:

- *imsize* = 5760
- *cycleniter* = 200 (or 100)
- *search_radius_arcsec* = 235.0

The reduction in search radius is required to keep the mosaic footprint within the full image, but this reduction also means that there will be a slight reduction in sensitivity at the edges of the inner degree. Note that these modifications are not always able to avoid divergence, particularly if the bright source is in the inner degree of the image and not excluded by the smaller image size, but even in these cases the reduction in *cycleniter* does usually cause the divergence to be slower, allowing deeper cleaning.

Because images can be made with non-standard parameters as described above, interested survey users can look at the entries in the *hif_editimlist* stage of the imaging pipeline weblog (available from the archive).

As of CASA-5.5.0, the mosaic gridder has the option to set a *psfphasecenter* for PSF calculations. Initial tests of this have proved promising for reducing divergences. Further development of this idea to incorporate into pipeline heuristics is underway.

3.2.2. Issues: Ghost sources

“Ghost sources” result from erroneous delay centers (see § 2.3) being used in the correlator. Table 3 summarizes the different system issues (including the presence of pointing errors described in § 2.2). The Cases are as described in Table 1.

Cases I, IIIa, and IIIb exhibit the symptoms of visible fainter copies of brighter sources that are displaced in the mosaic image by the offset of the phase-center used and the one used in imaging. These appear “ahead” of the true source position in the OTF scan direction. For the VLASS, which scans in Right Ascension at fixed Declination, these offsets are in RA only in multiples of the field separation of 178.74'' for 0.9s field durations and our typical OTF scan rate of 3.31'/s.⁴

Cases of ghosts have been found with offsets of up to eleven phase-centers, though most often they appear with the single field offset of 178.74''. Ghosts with offsets of more than nine phase-centers ($\sim 26'$) are not usually visible in the mosaic as they are far out in the

⁴By Tier: T01 1.91'/s; T02 2.32'/s; T03 2.69'/s; T04 2.97'/s; T05 3.15'/s; T06–T32 3.31'/s.

Primary Beam (used to weight the data in the mosaic) and thus are only found in single-field images made to search for ghosts in suspect regions (e.g. along with visible ghosts with smaller offsets).

Ghosts are identified by making the set of initial QL images for the entire tile (as ghost images can appear across image boundaries), after which component lists are created using PyBDSF[3]. The ensemble of components found are searched to identify cases of fainter sources located at multiples of the single-field offset (for that Tier) from a brighter component (within a tolerance of $2''$). These cases are then investigated by making single-field images of each phase-center (containing two visibility integrations) and looking for clear evidence of ghosting. These fields are then flagged in the calibrated MS, and the affected images re-made. In addition, the new flags are saved with the archived calibration so that subsequent restorations of this data will not have these ghosts. Note that the identification of these ghost images requires there to be a sufficiently bright source in the affected fields, above the thresholds chosen in the execution of PyBDSF (5-sigma). Therefore, there may be residual ghosts remaining in the data and QL images that fall below these thresholds, and caution should be taken when using QL images to search for faint transients. In particular, even if no ghosts are visible, the data will add as noise in the mosaic and thus the flux densities of faint sources (which would have sub-threshold ghosts) will be depressed, in some cases by as much as 25%.

In addition to the ghosts visible in mosaics described above, the Out-of-Order command events due to the race condition (covered by cases II and III in Table 1) sometimes caused ghosting. For case IIa and IIb, the 11th Field from the start of an OTF row was correlated at the wrong position (from 10 seconds earlier, usually the backup scan before the first OTF field) in a way that was not just an offset in RA, and could be very far from the intended delay center. In these cases, images of the 11th Field show a ghost with a RA offset of $32.769'$ (11 offsets of 0.9s at nominal scan rate). Although this is so far out in the primary beams that the ghost images are suppressed by the mosaic imaging algorithm and thus not visible in the mosaic QL images, this will act as a blank noise-only field when added in with the other fields. The effect of the inclusion of these blank fields in the QL images is to slightly depress the flux densities measured for sources at these locations.

For Case IIIb, OOO events corresponded to more extensive ghosting during the first 11 fields of the OTF row, though the 11th field itself is not always ghosted (unlike for IIb). Furthermore, there were ghosts seen that did not correspond to logged OOO events, yet appeared within the first 11 fields of an OTF row. See § 3.2.2 below for the statistics.

We investigated in detail a small number of events from Cases IIIb and IIb. This involved making single-field images from the first 12 fields of the corresponding OTF rows. The results of this are described below in Appendix A.

We note that for ghosts with offsets of around 8 or more fields, the Declination of the ghost tended away from the Declination of the parent source, in a direction toward the Celestial Equator. This includes the 11-th field case described above for OOO events. This offset increased with increasing field offset, and was seen to be more than $20''$ in some cases, rendering our ghost searches based upon RA-only offsets ineffective. Therefore, there may

be still cases of very faint ghosts remaining in Pilot and VLASS1.1 data that were not identified and eliminated. This effect is as yet unexplained. In § 2.3.1 and in Table 2 we describe the data flagging that was applied for the delay-related issues in SE imaging, as well as the status of flagging in the QL images.

Table 3: Summary of data affected by system issues in the Pilot, VLASS1.1, and VLASS1.2 data. The “Ghosts” column indicates whether ghost images are visible in mosaics, and the “OOO” column whether there are OOO events in the data. (Yes* in OOO means that these cases are logged). Noted in the final “Ptg” column is whether the pointing offsets (§ 2.2) are present. Time ranges and cases are as in Table 1.

Epoch	Date range	Case	Ghosts	OOO	Ptg
Pilot	2016-Jun-10 – Sep-01	I	Yes	No	No
1.1	2017-Sep-08 – Nov-14	I	Yes	No	Yes
1.1	2017-Nov-15 – 2018-Feb-20	IIa	No	Yes	Yes
1.2	2019-Mar-05 – Mar-14	IIa	No	Yes	No
1.2	2019-Mar-15 – Apr-11	IIIa	Yes	Yes	No
1.2	2019-Apr-12 – May-13	IIIb	Yes	Yes*	No
1.2	2019-May-14 – Jun-13	IIb	No	Yes*	No
1.2	2019-Jun-14 – present	IV	No	No	No

Occurrence rate of Ghosting events

In Table 4 we compile the statistics of ghost-related delay error events as described above. Logging of OOO events was only available after 2019-Apr-11, and thus only in cases IIIb, IIb, and IV do we have accurate estimates of rates (and case IV had no known events).

In the IIb period, we infer an event rate of around 3% per square degree. These are all logged OOO events, which in our testing seemed to consist of a distant (and non-visible) ghost in each case. These individually have low impact, as they only occur in a single field (the 11th of a OTF row). We might assume a similar rate for IIa in both VLASS1.1 and VLASS1.2 (where no ghosts are apparent).

For the IIIb data in Table 4, we infer an occurrence of ghost events of 0.072 deg^{-2} (391 events in 5418 deg^2). Note that in this case, only a fraction (half or less) of the OOO events exhibited ghosting when single fields were examined (albeit for only 10 cases), however when it did they showed extensive ghosting of up to the first 11 fields of the row. This will have a larger impact on the data. Furthermore, only 64.4% of the identified ghosts corresponded to OOO events. If we assume half of the OOO events correspond to true ghosting, and for each such ghost there are an additional 55.2% ghosts not in OOO, then the net true event count is 77.6% of that above (303.4 events) and we estimate a total rate of 0.056 deg^{-2} . In IIIb, all ghost cases (even if not associated with an OOO event)

occurred within the first 11 fields of an OTF row and thus affect only images on the east or west edges of a tile. Thus, the occurrence rate for these square degree edge images is $\sim 5\times$ higher, or around 28%.

Another estimation of the event rate in Case IIIb comes from the effective rate per OTF row of 0.0845 (303.4 in 3592 rows). Each ($62' \times 62'$) image on a tile edge contains nine OTF rows (spaced $7.2'$) of which, on average, will contain the start of an OTF row. Therefore, the estimated ghosting event rate for one of these images is

$$1 - (1 - 0.0845)^{4.5} = 0.328 \quad (1)$$

and roughly 33% of edge images will be affected.

These high rates and the possibility of unlogged events have informed our decision to flag OTF Field 11 in Case II, and OTF Fields 1–11 for Case III, in every OTF row regardless of whether we have logs for specific OOO events (IIb, IIIb). This is described above in § 2.3.1.

Table 4: Statistics of ghost events (INoV, Ghosts, OOO) in the Pilot, VLASS1.1, and VLASS1.2 data. Time ranges and cases are as in Table 3. Event types are as defined in Table 1. Here “Ghosts” refers to the total number of visible ghosts found in the mosaic images, “Ghost+OOO” refers to the subset of Ghost events where the visible ghosts fall within the first 11 fields of a logged OOO event, and “OOO” are the total number of OOO events logged. For the INoV and Ghost events, if present, the first number is the number of incidents (ranges of consecutive fields), with the total number of fields affected given in parentheses. For the OOO column, the first number is the number of logged OOO events (row starts) with the total number of OTF rows in the period in parentheses. The Rate is reported as total events per square degree (* denotes that the OOO rate is unknown).

Epoch	Case	Sq.Deg.	INoV	Ghosts	Ghost+OOO	OOO	Rate
Pilot	I	2480	82 (357)	7 (7)	–	– (3042)	0.036
1.1	I	8356	73 (104)	11 (15)	–	– (7173)	0.010
1.1	IIa	8583	0	0	0	– (8548)	0.0*
1.2	IIa	762	0	0	–	– (623)	0.0*
1.2	IIIa	2734	4 (4)	44 (137)	–	– (2113)	0.018*
1.2	IIIb	5418	0	45 (125)	29	346 (3592)	0.072
1.2	IIb	3604	0	0	0	103 (3093)	0.029
1.2	IV	4425	0	0	0	0 (4734)	0.0

Note that the rates for events given in Table 4 are significantly less than those for 5-sigma

noise excursions. For VLASS, there are approximately 2.6M resolution elements per square degree, and 5-sigma for Gaussian noise implies a false occurrence rate of approximately 1 in 3.5M resolution elements, or a rate of 0.74 per square degree.

3.2.3. Issue: Pointing Offsets

As described in § 2.2, for VLASS1.1 there were erroneous pointing offsets introduced into the system during observation of OTF scans. The data affected by this issue is indicated in the “Ptg” column of Table 3.

This error can only be corrected during imaging by application of these offsets in the Primary Beam location during the gridding and degriding process (in the CASA task *tclean* using the *gridding*=‘*mosaic*’ or ‘*awproject*’ options). For Quick-Look imaging, these were not applied, and thus all of the VLASS1.1 QL images are affected by this issue (see below). For SE imaging, these offsets will be corrected for using *gridding*=‘*awproject*’.

The primary effect on the QL images from the VLASS1.1 pointing errors is that the flux densities will be incorrect at the 10–15% level (see § 3.3.2).

3.2.4. Issue: W-Term

A limitation of using the *gridding*=‘*mosaic*’ in *tclean* is that the “w-term” in the interferometer equation (due to non-coplanarity of the projected baselines for the gridded image away from the phase center) is not corrected for in imaging as it is using *gridding*=‘*awproject*’. This w-term introduces a direction-dependent PSF in single-field images, with a characteristic distortion and position offset that grows with distance from the phase center. In mosaic images made from data combined from multiple fields (phase-centers), this manifests mainly as net position offsets of component centroids that depend upon the orientation of the array (with hour angle and declination) in the observations. There is also a small increase in the apparent sizes of compact sources (and corresponding depression of the peak flux density), though this is at most only a few percent for VLASS (the 1st Taylor-term (tt1) images used to estimate spectral indices are more strongly affected, but are not created by the QL pipeline). These w-term effects are characterized below (§ 3.3.1) and modeled in detail in VLASS Memo 14.

3.3. Quick Look image quality

Quick Look images are relatively fast to produce, but suffer from inaccuracies in both position and flux density, due to the issues described above. In order to quantify the uncertainties in flux density and position in the QL images, we used a number of techniques. First, we made use of re-observations on individual tiles. Several tiles were covered twice during the VLASS1.1 observations: in one case the Moon was accidentally observed in the tile (T14t05), and two (T09t02 and T09t35) were re-observed due to gain compression from RFI, but were later successfully recovered. In the pilot, several tiles were purposefully observed multiple times. For this analysis we used the images made of the Chandra

Deep Field South (CDFS), for which an observation tile was repeated three times. These duplicate observations were used for consistency and validation checks on the QL imaging. Second, we matched catalogs generated by PyBDSF over the entire VLASS1.1 and VLASS1.2 datasets to Gaia DR2, to investigate issues with positional accuracy. Third, we compared the flux densities and positions of calibrators recovered from the QL mosaics to their values from the pointed observations used to derive the calibrations. Finally, we also compared the flux densities of less variable calibrators to their values from the literature as a check on the absolute flux density calibration.

3.3.1. Quick Look positional accuracy

As described in detail in VLASS Memo 14, and shown in Figure 1, there is a significant offset between the sources in the original VLASS Epoch 1 QL images and their *Gaia* and VLBI cross-matches. Tests using *gridder='awproject'* and *wprojplanes* ≥ 16 showed greatly reduced position offsets. VLASS Memo 14 identifies the offsets as being due to wide-field effects from the different projections of the array across the primary beam, and derives an analytic correction that can be applied to the image WCS as a simple offset. The correction has been included in the QL pipeline for Epochs 2 and 3, and has been retroactively applied to Epoch 1 (in the VLASS1.1v2, VLASS1.2v2 directories in the NRAO VLASS cache website and also available through CADC; note that, for technical reasons related to product versioning, the Epoch 1 images in the NRAO archive access tool are currently (as of 5/31/22) the uncorrected images). After correction, the QL positions are as good as those in the SE images, with systematic errors ≈ 0.2 arcsec for Dec. > -30 deg., ≈ 0.3 arcsec for Dec. < -30 deg. and random errors $\approx 1.5/\rho$ arcsec, where ρ is the SNR of the source.

3.3.2. Quick Look flux density accuracy

We compared the measured flux densities of 56 calibrator sources that lie within the VLASS1.1 QL images, and 51 that lie within VLASS1.2 QL images with their flux densities derived from the pointed calibrator observations made during the observations of the same scheduling blocks. Any differences in the recovered flux densities should thus be dominated by the effect of the QL imaging algorithm, the online pointing offset bug that affected only the OTF data in VLASS1.1, and residual phase and amplitude errors in the calibration. As Figure 3 shows, there is a systematic offset of about 15% in peak flux densities and 10% in total flux densities between the calibrator flux density measurements in VLASS1.1 as derived from the pointed calibration observations, and those measured (using the CASA *imfit* task) in the QL images, in the sense that the QL flux densities are low. The differences for VLASS1.2 are significantly smaller, only 8% in the peak flux densities and 3% in the total.

To quantify issues with fainter sources, the peak flux densities in the QL images of the two VLASS1.1 observations of the tile T14t05 were compared. This comparison showed a scatter in the ratio of peak flux densities with a systematic periodicity with Dec at about

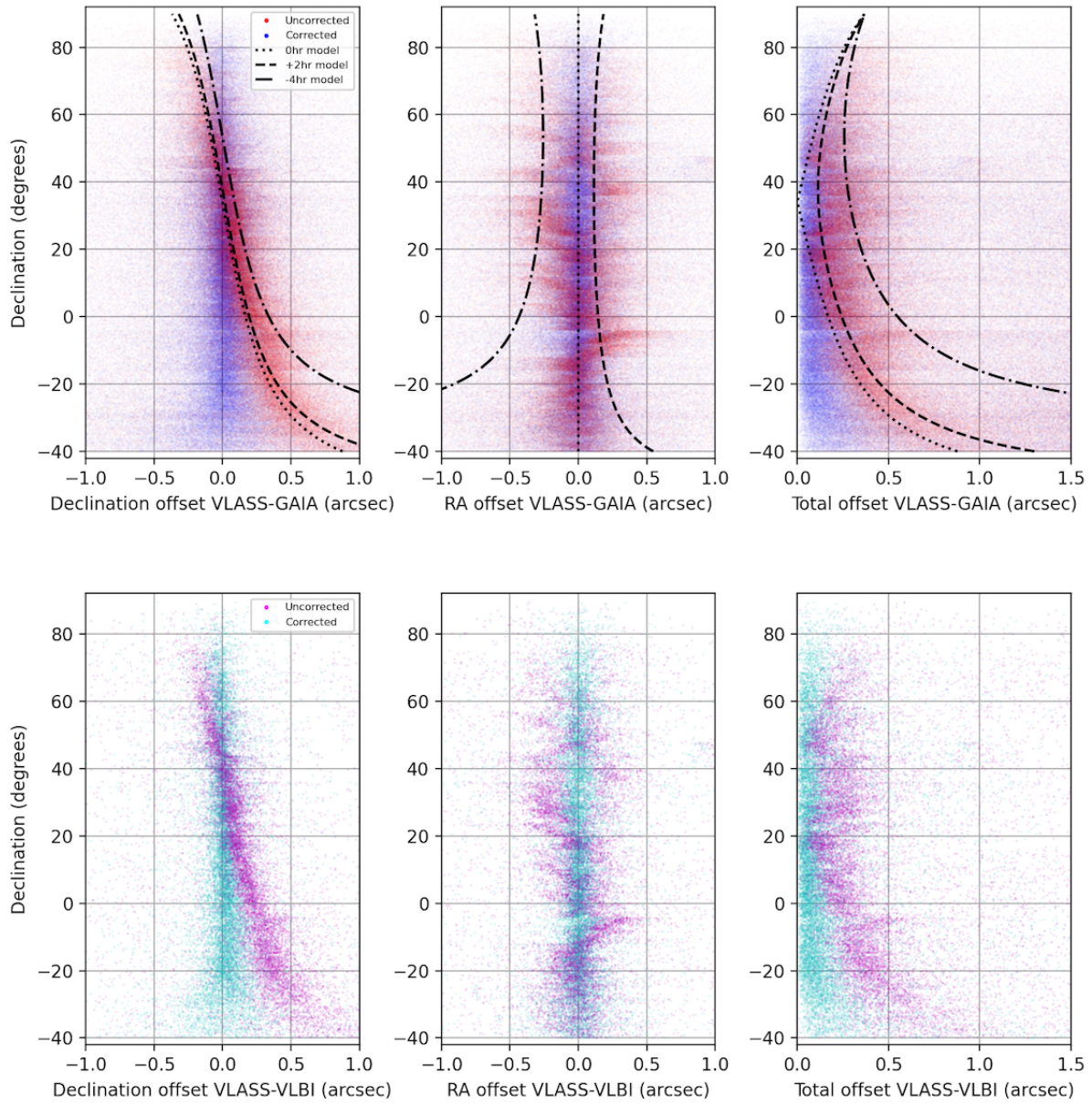


Figure 1: Positional offsets before and after the correction described in VLASS Memo 14 compared to Gaia EDR3 (top row) and the VLBI position reference catalog (see VLASS Memo 14 for details). Both rows: *Left*: Declination offset versus Declination, *middle*: Right Ascension offsets versus Declination, *right*: total offset versus Declination.

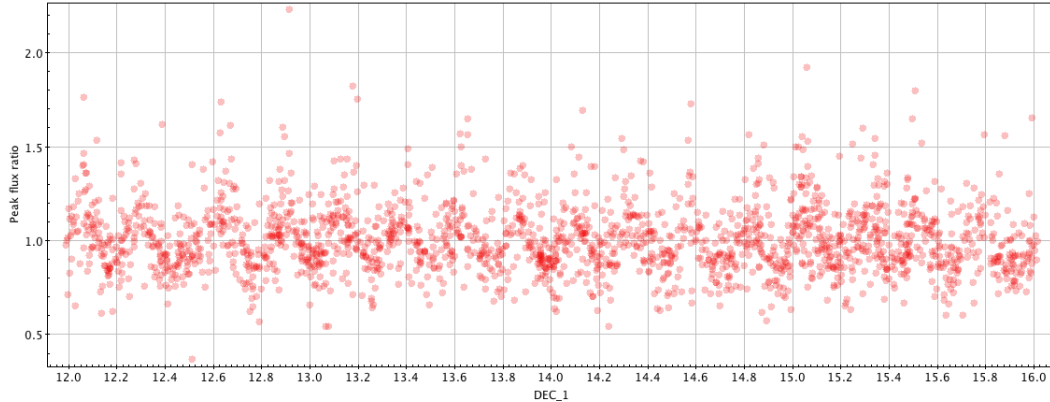


Figure 2: Peak flux ratio as a function of declination for two observations of tile T14t05 in VLASS1.1. The flux ratio appears periodic, with a peak-to-peak distance corresponding to ≈ 0.24 deg (two row spacings) and an amplitude of $\pm 15\%$. This is consistent with the known antenna pointing errors in VLASS1.1.

the 15% level, with a period corresponding to about twice the OTF row spacing (Figure 2). No such trend is seen in the ratio of total flux densities, but again, even for bright sources, the flux densities have a scatter of about 15%.

The ratio of peak flux densities of sources observed in the repeat observations that comprise the pilot data in CDFS shows no periodicity with Dec, and the scatter shows a significantly lower level of systematic uncertainty, with only 5% scatter in the flux ratios for objects with flux densities > 10 mJy. In terms of overall offsets, the flux densities of the first and third epochs of the CDFS field (which were taken at close to the same hour angle) are the same to within 1%, however, those in the second epoch are lower by about 8% than those in the first and third epochs. The cause(s) of the effects described above are under investigation.

In order to check the overall flux density scale, a comparison of the flux densities of six calibrators in a Australia Telescope Compact Array (ATCA) calibrator monitoring program [5] that had low variability at 2.5 GHz ($\leq 3\%$) and were present in the VLASS1.1 QL images (J0503+0203, J1150–0023, J1501–3918, J2110–1020, J2129–1538 and J2346+0930) was performed. The mean flux ratio between the VLASS flux densities and those of the ATCA calibrators is 0.98 ± 0.04 (after correction of the 2.5 GHz fluxes to 3.0 GHz using the spectral indices in [5]) with a range of 0.84–1.13. These observations were calibrated using observations of PKS 1934–638, using its flux density from Reynolds (1994)⁵.

These comparisons show that there are significant uncertainties associated with the flux densities derived from the VLASS1.1 QL images, both in terms of scatter and an average offset relative to the current Perley-Butler flux density scale [4], in the sense that the recovered flux densities from the QL images are (on average) low. VLASS1.2 is much

⁵<http://www.atnf.csiro.au/observers/memos/d96783~1.pdf>

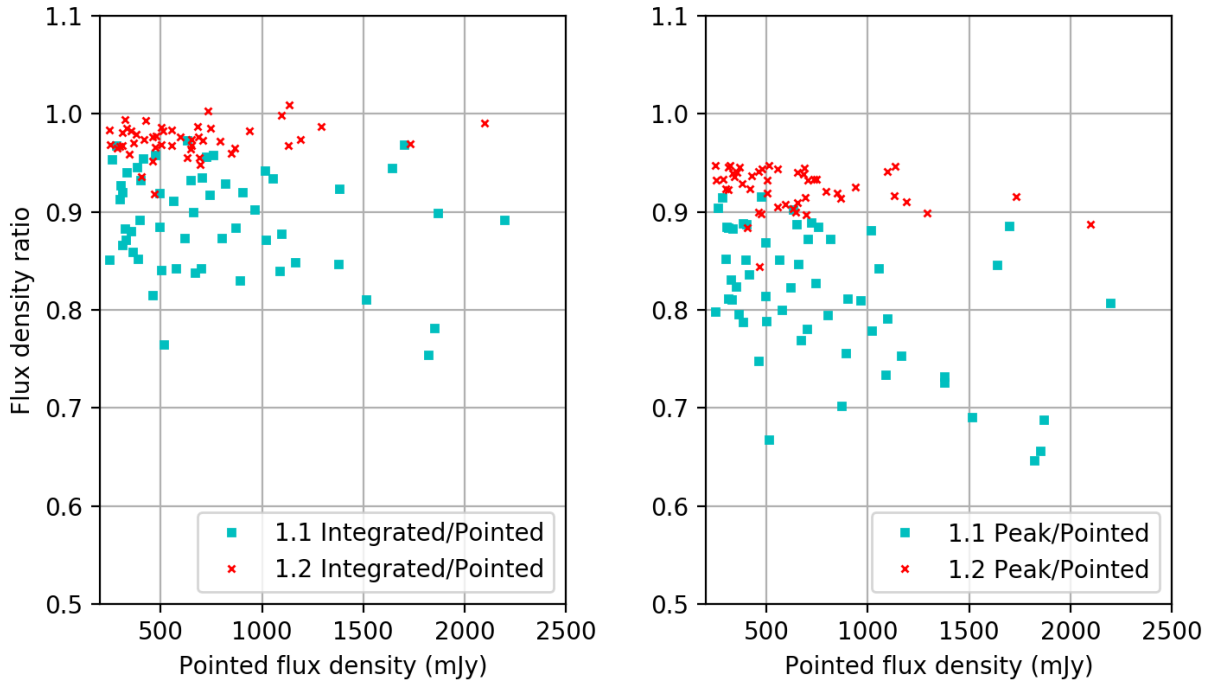


Figure 3: Ratios of measured flux densities on Epoch 1 QL images to flux density estimates based on the pointed observations of the calibrators used for gain calibration. *Left:* the ratios of integrated flux densities from the QL images to the pointed values, *right:* the ratios of peak flux densities relative to the pointed values. In both plots the VLASS 1.2 flux densities lie much closer to the pointed values than those from VLASS 1.1.

better, and, as described in VLASS Memo 17, once VLASS1.2 images are self-calibrated in the SE pipeline, the peak flux densities improve to match the total fluxes, and we show that the flux density scale is within 3% of Perley-Butler. **Note that we do not endorse the suggestion in Gordon et al. [1] to increase VLASS total flux densities by 15% for all Epoch 1 observations (though for VLASS1.1 only an $\approx 10\%$ correction is appropriate).**

3.3.3. Sensitivity

The effective integration time for a given position on the sky for VLASS is 5 seconds; taking into account the measured System Equivalent Flux Density (SEFD) across the 2–4 GHz

band, and assuming 1500 MHz of RFI-free bandwidth, the theoretical sensitivity should be $\sim 120 \mu\text{Jy}/\text{beam}$. Taking into account the approximations used when creating the QL images, the survey system requirement is for the RMS noise in the QL images to be better than $200 \mu\text{Jy}/\text{beam}$ over at least 80% of the observed sky. Using the noise images described in Section 3.1.2 we find that for VLASS1.1 this requirement is met for 96% of the observed sky, and furthermore, that 93% of the pixels are within 40% of the theoretical sensitivity (i.e., less than $168 \mu\text{Jy}/\text{beam}$).

3.3.4. Quick Look image artifacts

The algorithms used to generate the Quick Look images were designed to run quickly, in particular to allow searches for transient radio sources. This means that, in addition to the minor issues described above, some images are affected by systematic failures in the clean algorithm and/or poor phase calibration.

Bright sources: there is a systematic variation in the PSF across a VLASS mosaic that is not allowed for in the clean. Thus, the presence of bright ($> 100 \text{ mJy}$) sources with high S:N sidelobes can sometimes cause the clean algorithm to diverge. For the most part these fields are found during QA and typically they are placed in the QA rejected category if the ratio of the residual from the clean to the RMS over the remainder of the image exceeds 10:1, but in general users should exercise caution when extracting detections of faint objects in the vicinity of bright ones, as false detections and/or distorted morphologies are likely to be found.

Phase errors: no self-calibration is applied to the Quick Look images. Thus, their dynamic range is very dependent on observing conditions. This typically leads to depressed peak flux densities by 5-10% and small position errors $\approx 0.1 \text{ arcsec}$. In the worst cases, phase errors can lead to a false impression that an object has a particular morphology or size. As the phase errors will persist over a large fraction of a tile, the keys to identifying these is that all point-like sources share a morphology, and the distortions around the point sources are asymmetric in nature. Quantitatively, the near-field dynamic range 8-arcsec ($\approx 3 \text{ beams}$) from a point source (defined as the ratio of the peak brightness in the center to the magnitude of the largest artifact on an $8''$ radius circle) ranges from about 10:1 to 100:1 in the Quick Look images. At the lower end of this range, particularly when using a logarithmic or histogram stretch in a viewer, it is easy to mistake such artifacts for real morphological features. An example of such an unusually poor image is shown in Figure 4.

4. Summary

The Quick Look image products from the VLA Sky Survey are designed to be produced quickly for the purpose of transient identification. They therefore lack the accuracy and dynamic range of images that include self-calibration. Furthermore, a problem with the

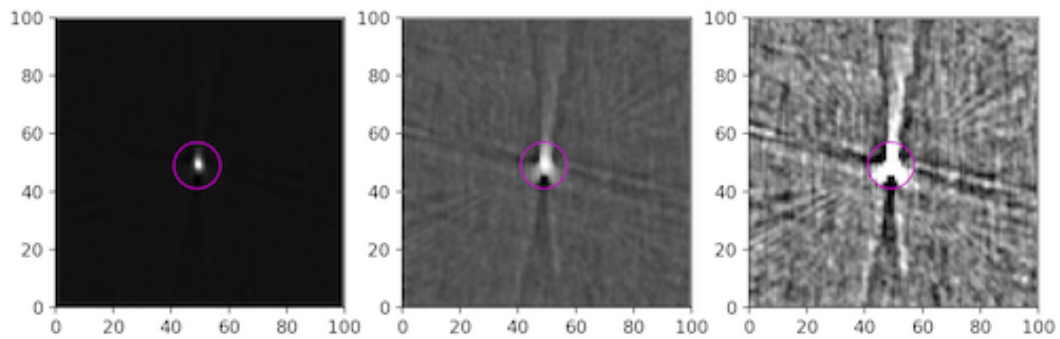


Figure 4: A point source in a tile with poor image quality. Left: a linear stretch from the image minimum to maximum, center: a logarithmic stretch from minimum to maximum, and right a ± 5 -sigma stretch, where the rms, sigma, is measured in the image far from bright sources. Note the characteristic three-fold pattern, asymmetric about the source center. The magenta circle shows the 8" radius used for calculating the near-field dynamic range. In this example, the value of the near-field dynamic range is 13.

antenna pointing information in VLASS1.1 added systematic errors in the flux densities for those observations. In Epoch 1, online system errors during observing created both “ghost sources” and sources missing flux density due to the ghost source phenomenon. Therefore, users requiring high accuracy in source measurements should use these QL products with great caution. The VLASS Single-Epoch images (continuum wideband intensity and spectral index, and coarse intensity and polarization cubes) will be better-suited for use cases that require high precision.

We summarize these issues, as well as general features relevant to VLA snapshot observations, below in the context of the use of the VLASS Pilot and Epoch 1 Quick-look images for research:

Flux Density Accuracy: For flux densities below ≈ 1 Jy, the peak flux densities in VLASS1.1 are systematically low by $\approx 15\%$, and the total flux densities by $\approx 10\%$, with a systematic scatter of $\approx \pm 8\%$. Above 1 Jy the VLASS1.1 flux densities can be very unreliable and should not be used. The other observing campaigns (VLASS1.2, VLASS2.1 and VLASS2.2) have total flux densities accurate to within 3% and peak fluxes to $\approx 5 - 10\%$. Occasionally, however, for any Epoch 1 sources that happen to be located near a region that was affected by uncorrected Ghost phenomena, flux densities could be low by as much as 25%.

Sensitivity to Extended Emission: The shortest baselines covered by S-band B-array are approximately $58''$ (see the Largest Angular Scale (LAS) in Table 3.1.1 in the Observational Status Summary⁶). On those scales the recovery of extended emission will vary with morphology, but we see typically 20% flux errors when compared to C-configuration observations (see the SE continuum image release notes, VLASS Memo 19). In addition, the QL images were made by combining data over the full 2–4 GHz band during imaging, resulting in a factor of two in scale over the band with an uncertain impact on the LAS for these wideband images. We have no quantitative assessment at this time on the sensitivity and accuracy of the VLASS QL images to extended structure, and we caution users to keep this in mind when using these images.

Ghost Artifacts: As described in § 2.3 and § 3.2.2, there were errors during Epoch 1 observing that caused faint “ghost” copies of sources to appear at multiples of 1 or more field offsets ($178.74''$ in most Tiers) in RA. Although we have identified and removed cases of this where our source finding could identify these in the mosaic images (requiring 5-sigma detection of the fainter ghost image), there are undoubtedly cases of this still in the QL images that fell below our detection threshold. Even if the ghosts are too faint to see in an image, they will cause redistribution of flux density away from a true source, biasing its measured flux density to a lower value. These ghost remnants would be from observations made in the Pilot, VLASS1.1 before 2017-Nov-15, and in VLASS1.2 between 2019-Mar-13 and May-13. VLASS QL users are recommended to check components of interest during these times for the effects of faint ghosts, for example when looking for binary AGN or double sources.

⁶<https://science.nrao.edu/facilities/vla/docs/manuals/oss>

References

- [1] Yjan A. Gordon, Michelle M. Boyce, Christopher P. O’Dea, Lawrence Rudnick, Heinz Andernach, Adrian N. Vantyghem, Stefi A. Baum, Jean-Paul Bui, Mathew Dionyssiou, Samar Safi-Harb, and Isabel Sander. A Quick Look at the 3 GHz Radio Sky. I. Source Statistics from the Very Large Array Sky Survey. *Astrophysical Journal Supplement Series*, 255(2):30, August 2021.
- [2] M. Lacy, S. A. Baum, C. J. Chandler, S. Chatterjee, T. E. Clarke, S. Deustua, J. English, J. Farnes, B. M. Gaensler, N. Gugliucci, G. Hallinan, B. R. Kent, A. Kimball, C. J. Law, T. J. W. Lazio, J. Marvil, S. A. Mao, D. Medlin, K. Mooley, E. J. Murphy, S. Myers, R. Osten, G. T. Richards, E. Rosolowsky, L. Rudnick, F. Schinzel, G. R. Sivakoff, L. O. Sjouwerman, R. Taylor, R. L. White, J. Wrobel, H. Andernach, A. J. Beasley, E. Berger, S. Bhatnager, M. Birkinshaw, G. C. Bower, W. N. Brandt, S. Brown, S. Burke-Spolaor, B. J. Butler, J. Comerford, P. B. Demorest, H. Fu, S. Giacintucci, K. Golap, T. Güth, C. A. Hales, R. Hiriart, J. Hodge, A. Horesh, Ž. Ivezić, M. J. Jarvis, A. Kamble, N. Kassim, X. Liu, L. Loinard, D. K. Lyons, J. Masters, M. Mezcua, G. A. Moellenbrock, T. Mroczkowski, K. Nyland, C. P. O’Dea, S. P. O’Sullivan, W. M. Peters, K. Radford, U. Rao, J. Robnett, J. Salcido, Y. Shen, A. Sobotka, S. Witz, M. Vaccari, R. J. van Weeren, A. Vargas, P. K. G. Williams, and I. Yoon. The Karl G. Jansky Very Large Array Sky Survey (VLASS). Science Case and Survey Design. *Publications of the Astronomical Society of the Pacific*, 132(1009):035001, March 2020.
- [3] N. Mohan and D. Rafferty. PyBDSF: Python Blob Detection and Source Finder. Astrophysics Source Code Library, February 2015.
- [4] R. A. Perley and B. J. Butler. An Accurate Flux Density Scale from 50 MHz to 50 GHz. *The Astrophysical Journal Supplement Series*, 230:7, May 2017.
- [5] S. J. Tingay, D. L. Jauncey, E. A. King, A. K. Tzioumis, J. E. J. Lovell, and P. G. Edwards. ATCA Monitoring Observations of 202 Compact Radio Sources in Support of the VSOP AGN Survey. *Publications of the Astronomical Society of Japan*, 55:351–384, April 2003.

A. Case Studies for Out-of-Order (OOO) Events

A.1. Case IIIb

There were two datasets studied from Case IIIb which had the erroneous CMIB code version and logged OOO events from the executor.

- 9 race conditions logged:

- 3 with extensive ghosting (more than 11th field). All 3 show 11th ghosted (at 11x offset of 9.9s equivalent), of which two had visible ghosts previously identified from mosaic images
 - 5 with confirmed as having no ghosts for first 12 fields
 - 1 ambiguous (no ghost in some fields, rest no sources visible to test)
 - 1 ghost identified from mosaic w/o logged OOO race condition — single phase center with source and ghost present
- Assessment:
 - > 50% of race conditions show no ghosting (including 11th field)
 - ~ 40% of race conditions show classical ghosts, including 11th field (11x offset). Ghosting is more extensive than found in first search, may need to expand/refine search for SE processing
 - no cases of race conditions with only 11th field as 11x ghost (post-CMIB rollback pathology)
 - 3 visible ghosts found previously — 2 (67%) correspond to OOO, one case (33%) of loner visible ghost without OOO race condition logged. This is similar rate to that seen in full IIIb statistics.

VLASS1.2_T20t09.T20t12.T20t15_P48582v3_2019_05_04T16_51_48.242:

SBID: VLASS1.2.sb36618589.eb36641469.58607.077784375

Observed: from 04-May-2019/01:52:01.6 to 04-May-2019/07:42:49.5 (UTC)

Previously identified issues:

- (T20t09) fields 3898–3903 flagged due to visible ghosting
- (T20t12) fields 8512–8516 flagged due to visible ghosting

Logged OOO events:

- OOO received MJD 58607.137371 (2019-05-04T03:17:49.650Z to 2019-05-04T03:17:58.750Z)
Summary: first 11 fields 3898–3908 all ghosted (flag all these, including 11th 3908).
Mosaic Image: VLASS1.2.ql.T20t09.J071050+383000.10.2048.v1
- OOO received MJD 58607.169548 (2019-05-04T04:04:09.750Z to 2019-05-04T04:04:18.850Z)
Summary: no ghosts seen (including the 11th field 6560), no flagging needed. Mosaic Image: VLASS1.2.ql.T20t12.J093414+363000.10.2048.v1
- OOO received MJD 58607.192433 (2019-05-04T04:37:07.050Z to 2019-05-04T04:37:16.150Z)
Summary: first 11 fields 8512–8522 ghosted (flag all these, including 11th 8522). Mosaic Image: VLASS1.2.ql.T20t12.J093432+373000.10.2048.v1

- OOO received MJD 58607.227095 (2019-05-04T05:27:01.800Z to 2019-05-04T05:27:10.900Z)
Summary: no ghosts seen (including the 11th field 11597), no flagging needed. Mosaic Image: VLASS1.2.ql.T20t12.J093509+393000.10.2048.v1
- OOO received MJD 58607.267371 (2019-05-04T06:25:01.650Z to 2019-05-04T06:25:10.750Z)
Summary: no ghosts seen (including the 11th field 14994), no flagging needed. Mosaic Image: VLASS1.2.ql.T20t15.J111432+383000.10.2048.v1
- OOO received MJD 58607.269438 (2019-05-04T06:28:00.300Z to 2019-05-04T06:28:09.400Z)
Summary: no ghosts seen (including the 11th field 15184), no flagging needed. Mosaic Image: VLASS1.2.ql.T20t15.J115850+383000.10.2048.v1
- OOO received MJD 58607.278454 (2019-05-04T06:40:59.250Z to 2019-05-04T06:41:08.350Z)
Summary: 2nd–7th fields not ghosted, no other sources visible to check other fields. Ambiguous case. Mosaic Image: VLASS1.2.ql.T20t15.J115850+383000.10.2048.v1

VLASS1.2_T07t05.T08t05_P44576v2_2019_04_28T20_30_22.012:

SBID: VLASS1.2.sb36442551.eb36615607.58601.73545628472

Observed: from 28-Apr-2019/17:39:04.9 to 28-Apr-2019/21:49:41.7 (UTC)

Previously identified issues:

- (T07t05) field 2387 flagged due to visible ghosting

Logged OOO events:

- OOO received MJD 58601.770324 (2019-04-28T18:29:16.800Z to 2019-04-28T18:29:25.900Z)
Summary: Fields 1396–1399 no ghosts, flag fields 1400–1406 for ghosts (incl. 11th 1406). Mosaic Image: VLASS1.2.ql.T07t05.J031824-123000.10.2048.v1
- NO OOO - ghost identified from mosaic image. Summary: Field 2387 both ghost and source seen, no other ghosts (11th ok). Mosaic Image: VLASS1.2.ql.T07t05.J031828-133000.10.2048.v1
- OOO received MJD 58601.813949 (2019-04-28T19:32:06.000Z to 2019-04-28T19:32:15.100Z)
Summary: no ghosts seen Fields 5147–5157. Mosaic Image: VLASS1.2.ql.T07t05.J031838-153000.10.2048.v1

A.2. Case IIb

We investigated 15 logged OOO events found in 9 SBs from Case IIb where the executor race condition was present but the CMIB had been reverted to the version from that start of VLASS1.2 (before ghosting was seen). For this testing, we made single-field images of the first 12 fields of the OTF row corresponding to the event.

- Cases investigated: 15 (from 9 SBs)

- Cases of OOO with 11th field ghost seen: 15
- Cases of OOO with 11th field correct: 0
- Cases of OOO could not see any sources: 0
- Cases of ghosting in fields other than the 11th OTF field of the row: 0
- Assessment:
 - 15/15 cases the 11th field (and only the 11th field of the first 12) of the OTF row containing the OOO event showed ghosting.
 - The DEC offsets were not as expected (near zero) and were offset toward the equator. We have no explanation for this.
 - No examples of these ghosts were seen in the mosaic image, likely due to the suppression by the primary beam during imaging.
 - Only investigated one row with bright source and no OOO logged, it did not show any ghosts (11th field was correct).
 - It seems likely that all logged OOO events correspond to 11th field ghosts, and likely (given the known pathology in the executor software) that only the 11th field of an OTF row during this period is affected.
 - Cannot discount that there were 11th field ghosts for times without logged OOO events during this period.

VLASS1.2_T11t19.T10t19_P42317v1_2019_05_14T08_01_53.371

SBID: VLASS1.2.sb36550623.eb36654876.58617.1435291088

- OOO received MJD 58617.159194 (2019-05-14T03:49:15.150Z to 2019-05-14T03:49:24.250Z)
Summary: Field 218 ghost at 12:03:55.694 +00.04.22.345 offset RA=32.84' (9.92s)
DEC=-6.59" (source at 12:01:44.3425 +00.04.28.9321). Mosaic Image: VLASS1.2.ql.T11t19.J120200
- OOO received MJD (58617.301918 : 2019-05-14T07:14:46.500Z : 2019-05-14T07:14:55.600Z)
Summary: Field 12601 ghost at 12:35:32.3680 -03.28.55.8720 offset RA=-32.93' (-9.95s) DEC=-8.53" (source at 12:37:44.3169 -03.28.47.3445). Mosaic Image: VLASS1.2.ql.T10t19.J1033000.10.2048.v1

VLASS1.2_T21t05.T22t05_P45245v1_2019_05_14T20_12_59.620

SBID: VLASS1.2.sb36565730.eb36654965.58617.61972854167

- OOO received MJD 58617.662970 (2019-05-14T15:54:41.400Z : 2019-05-14T15:54:50.500Z)
Summary: Field 1340 ghost at 04:53:53.0092 +43.08.38.1367 offset RA=-32.59' (-9.84s) DEC=-22.96" (source at 04:56:51.6464 +43.09.01.0937) Mosaic Image: VLASS1.2.ql.T21t05.J1033000.10.2048.v1

VLASS1.2_T24t07.T23t07.T23t11_P39804v1_2019_05_14T05_13_01.606

SBID: VLASS1.2.sb36400295.eb36657478.58617.88126371527

- OOO received MJD 58617.906944 (2019-05-14T21:46:00.750Z to 2019-05-14T21:46:09.850Z)
Summary: Field 856 ghost at 06:07:24.339 +56.19.16.028 (source at 06:03:28.338 +56.19.37.400) Mosaic Image: VLASS1.2.q1.T24t07.J060334+563000.10.2048.v1
- OOO received MJD 58617.969210 (2019-05-14T23:15:40.500Z to 2019-05-14T23:15:49.600Z)
Summary: Field 6175 ghost at 06:06:51.015 +52.42.48.267 offset RA=32.72' (9.89s)
DEC=-21.32" (source at 06:03:14.9442 +52.43.09.5895) Mosaic Image: VLASS1.2.q1.T24t07.J060314
- OOO received MJD 58618.071183 (2019-05-15T01:42:31.050Z to 2019-05-15T01:42:40.150Z)
Summary: Field 14915 ghost at 10:06:42.732 +51.17.59.517 offset RA=32.80' (9.91s)
DEC=-19.78" (source at 10:03:13.4449 +51.18.19.3014) Mosaic Image: VLASS1.2.q1.T23t11.J100310

VLASS1.2_T09t15.T09t18_P42728v1_2019_05_16T07_01_00.466

SBID: VLASS1.2.sb36552935.eb36659605.58619.10333078704

- OOO received MJD 58619.246709 (2019-05-16T05:55:16.500Z to 2019-05-16T05:55:25.600Z)
Summary: Field 11139 ghost at 11:56:27.1986 -05.22.33.1664 offset RA=-32.80' (-9.91s) DEC=-7.04" (source at 11:58:38.975 -05.22.26.13) Mosaic Image: VLASS1.2.q1.T09t18.J11580.053000.10.2048.v1

VLASS1.2_T17t28.T17t32_P49060v3_2019_05_16T14_39_47.405

SBID: VLASS1.2.sb36628882.eb36659653.58619.39739650463

- OOO received MJD 58619.485491 (2019-05-16T11:39:07.200Z to 2019-05-16T11:39:16.300Z)
Summary: Field 5964 ghost at 20:55:23.391 +24.23.53.817 offset RA=-32.78' (-9.90s)
DEC=-9.86" (source at 20:57:47.3634 +24.24.03.6794) Mosaic Image: VLASS1.2.q1.T17t28.J205923+

VLASS1.2_T22t08.T21t08_P47124v1_2019_05_16T23_01_55.458

SBID: VLASS1.2.sb36609824.eb36660158.58619.736312395835

- OOO received MJD 58619.839866 (2019-05-16T20:09:25.200Z to 2019-05-16T20:09:34.300Z)
Summary: Field 7477 ghost at 07:05:10.616 +40.14.32.374 offset RA=32.92' (9.95s)
DEC=-15.73" (source at 07:02:18.0883 +40.14.48.1000) Mosaic Image: VLASS1.2.q1.T21t08.J070236
Notes: reimaged after flagging 7477 and 8635, source flux density new/old 1.047x.
Check fields up to 1501, no further ghosts seen.
- OOO received MJD 58619.853204 (2019-05-16T20:28:37.650Z to 2019-05-16T20:28:46.750Z)
Summary: Field 8635 ghost at 07:05:55.9164 +40.34.44.5858 offset RA=32.8584' (9.93s) DEC=-17.04" (source at 07:03:02.8657 +40.35.01.6299) Mosaic Image: VLASS1.2.q1.T21t08.J
Notes: reimaged after flagging 7477 and 8635, weak source new/old 1.0000x
- OOO received MJD 58619.897392 (2019-05-16T21:32:15.450Z to 2019-05-16T21:32:24.550Z)
Summary: Field 12493 ghost at 07:06:22.540 +042.57.54.478 offset RA=32.8263' (9.92s) DEC=-19.09" (source at 07:03:23.089 +042.58.13.566) Mosaic Image: VLASS1.2.q1.T21t08.J

VCLASS1.2_T17t26.T17t30_P48880v1_2019_05_17T12_13_10.598

SBID: VCLASS1.2.sb36627706.eb36662063.58620.307527881945

- OOO received MJD 58620.423428 (2019-05-17T10:09:45.000Z to 2019-05-17T10:09:54.100Z)
Summary: Field 8631 ghost at 22:25:36.554 +27.00.46.502 offset RA=-32.7341' (-9.89s) DEC=+104.8" (extended N-S multiple source brightest at 22:28:03.486 +26.59.01.646, position unreliable) Mosaic Image: VCLASS1.2.ql.T17t30.J222945+263000.10.2048.v1

VCLASS1.2_T24t02.T23t02_P46647v1_2019_05_17T16_48_59.182

SBID: VCLASS1.2.sb36589905.eb36662075.58620.48503118056

- OOO received MJD 58620.584777 (2019-05-17T14:02:05.550Z to 2019-05-17T14:02:14.650Z)
Summary: Field 7106 ghost at 01:53:47.707 +52.05.16.943 offset RA=-32.5812' (-9.84) DEC=-18.27" (source at 01:57:19.8243 +52.05.35.2165) Mosaic Image: VCLASS1.2.ql.T24t02.J010306+
- OOO received MJD 58620.633621 (2019-05-17T15:12:25.650Z to 2019-05-17T15:12:34.750Z)
Summary: Field 11287 ghost at 01:06:30.419 +50.24.48.171 offset RA=33.3736' (10.08s) DEC=-34.322" (source at 01:03:00.932 +50.25.22.493) Mosaic Image: VCLASS1.2.ql.T23t02.J010306+

VCLASS1.2_T21t23.T22t23_P49833v1_2019_05_19T13_37_15.551

SBID: VCLASS1.2.sb36651475.eb36670581.58622.36553387731

- OOO received MJD 58622.386569 (2019-05-19T09:16:40.350Z to 2019-05-19T09:16:49.450Z)
Summary: Field 235 ghost at 22:05:21.115 +43.50.41.559 offset RA=32.9526' (9.96s) DEC=-16.53" (source at 22:02:18.3400 +43.50.58.0843) Mosaic Image: VCLASS1.2.ql.T21t23.J220244
Notes: Ghost is clearly exact copy of an extended linear triple. The W component was measured.